Two types of magnetic shape-memory effects from twinned microstructure and magneto-structural coupling in $Fe_{1+y}Te$

Sahana Rößler[a,1], Cevriye Koz[a], Zhaosheng Wang[b,c], Yurii Skourski[b], Mathias Doerr[d], Deepa Kasinathan[a], Helge Rosner[a], Marcus Schmidt[a], Ulrich Schwarz[a], Ulrich K. Rößler[e], and Steffen Wirth[a,1]

[a]Max-Planck-Institut für Chemische Physik fester Stoffe, 01187 Dresden, Germany; [b]Hochfeld-Magnetlabor Dresden (HLD-EMFL), Helmholtz-Zentrum Dresden-Rossendorf, 01314 Dresden, Germany; [c]High Magnetic Field Laboratory, Chinese Academy of Sciences, Hefei, Anhui 230031, People's Republic of China; [d]Institut für Festkörper- und Materialphysik, Technische Universität Dresden, 01062 Dresden, Germany; and [e]Institute for Theoretical Solid State Physics, IFW Dresden, 01171 Dresden, Germany

Edited by Malcolm R. Beasley, Stanford University, Stanford, CA, and approved July 10, 2019 (received for review March 27, 2019)

A detailed experimental investigation of $Fe_{1+y}Te$ (y = 0.11, 0.12) using pulsed magnetic fields up to 60 T confirms remarkable magnetic shape-memory (MSM) effects. These effects result from magnetoelastic transformation processes in the low-temperature antiferromagnetic state of these materials. The observation of modulated and finely twinned microstructure at the nanoscale through scanning tunneling microscopy establishes a behavior similar to that of thermoelastic martensite. We identified the observed, elegant hierarchical twinning pattern of monoclinic crystallographic domains as an ideal realization of crossing twin bands. The antiferromagnetism of the monoclinic ground state allows for a magnetic-field–induced reorientation of these twin variants by the motion of one type of twin boundaries. At sufficiently high magnetic fields, we observed a second isothermal transformation process with large hysteresis for different directions of applied field. This gives rise to a second MSM effect caused by a phase transition back to the field-polarized tetragonal lattice state.

magnetic shape-memory effect | antiferromagnets | Fe-chalcogenides

The magnetic shape-memory (MSM) effects are well known in ferromagnetic materials such as Ni-Mn-Ga–based alloys (1, 2) or other Heusler compounds (3). The first type arises due to a field-induced reorientation of one of the crystallographic twin variants. The second type results from a metamagnetic reverse phase transformation. Both effects are rarely found in antiferromagnets because of the absence of a net magnetic moment (4, 5). In the antiferromagnetic parent compound of high-T_c cuprate $La_{2-x}Sr_xCuO_4$, a strong magnetic anisotropy owing to spin–orbit coupling, a mechanism through which the spin degrees of freedom couple to the lattice, is considered as a driving force for the MSM effect (4). It is generally believed that this first type of macroscopic shape effect by an applied magnetic field requires a twinned microstructure at a ferroelastic transition between a higher-symmetry austenite and a low-symmetry martensite phase (1, 2). The MSM effect of the first type consists of a rearrangement involving the growth of some twin domains at the expense of less-favored orientations. The detailed microscopic process in the case of the metamagnetic shape memory—the second type—requires a transformation between 2 different magnetic phases with different lattice geometries; i.e., it is a field analogue of a conventional temperature-driven shape-memory effect. However, the present understanding of the MSM behavior is incomplete and there is no consensus about which materials are expected to display these processes. Observation of both types of MSM effects in the same material is interesting, because it suggests that a high mobility of planar twin walls in the martensitic phase (for the first type) and that of the phase boundaries between 2 different magnetic phases (for the second type) may originate from similar features of the underlying different microstructure.

In the case of Fe-based high-T_c superconductors, magnetic-field–induced persistent detwinning has been reported (6–11). However, a clear physical picture of these detwinning processes including a quantitative theoretical analysis is still lacking. In this article, we provide a detailed identification of the actual microstructures and mechanisms responsible for these field-induced processes by performing magnetization and magnetostriction measurements in pulsed magnetic fields on single crystals of $Fe_{1+y}Te$ (y = 0.11 and 0.12), both in the twinned and in the mechanically detwinned state. In particular, our magnetostriction measurements up to a magnetic field of 60 T show that the spin reorientation (10) and magnetostructural transition (11) observed in $Fe_{1.11}Te$ are related to 2 different types of MSM effects. Fig. 1 summarizes these processes, as seen in the magnetization measurements up to 60 T (Fig. 1*A*). An initial hierarchical twinning (Fig. 1*A*, *Lower Left Inset*) of the monoclinic crystal is first transformed at H_{m1} into a single plate consisting only of 2 monoclinic twin variants, which is effectively a single-domain orthorhombic structure with nanotwinning (Fig. 1*A*, *Middle Inset*). At higher-field H_{m2} and in a second step, the monoclinic lattice structure is replaced by the

Significance

Magnetic shape memory (MSM) refers to a change in shape and/or size of a magnetic material upon applying a magnetic field. There are 2 types of MSM effects; the first one occurs in a twinned magnetically ordered material, in which the crystallographic axes are irreversibly reoriented by the applied magnetic field. In the second type, the applied field drives a magnetoelastic phase transition. In certain iron tellurides $Fe_{1+y}Te$, both types of MSM occur. Notably, the first antiferromagnetic compound found to display an MSM effect is a parent material to the well-studied high-T_c cuprate superconductor $La_{2-x}Sr_xCuO_4$. Observation of MSM effects in 2 known material families related to high-T_c superconductors points to a prominent role of electron–phonon coupling arising through the spin–orbit interactions.

Author contributions: S.R., U.K.R., and S.W. designed research; S.R., C.K., Z.W., Y.S., M.D., D.K., H.R., and U.K.R. performed research; C.K., M.S., and U.S. contributed new reagents/analytic tools; S.R., C.K., Z.W., Y.S., M.D., D.K., H.R., and U.K.R. analyzed data; and S.R., U.K.R., and S.W. wrote the paper.

The authors declare no conflict of interest.

This article is a PNAS Direct Submission.

[1]To whom correspondence may be addressed. Email: roessler@cpfs.mpg.de or Steffen.Wirth@cpfs.mpg.de.

This article contains supporting information online at www.pnas.org/lookup/suppl/doi:10.1073/pnas.1905271116/-/DCSupplemental.

Published online August 7, 2019.

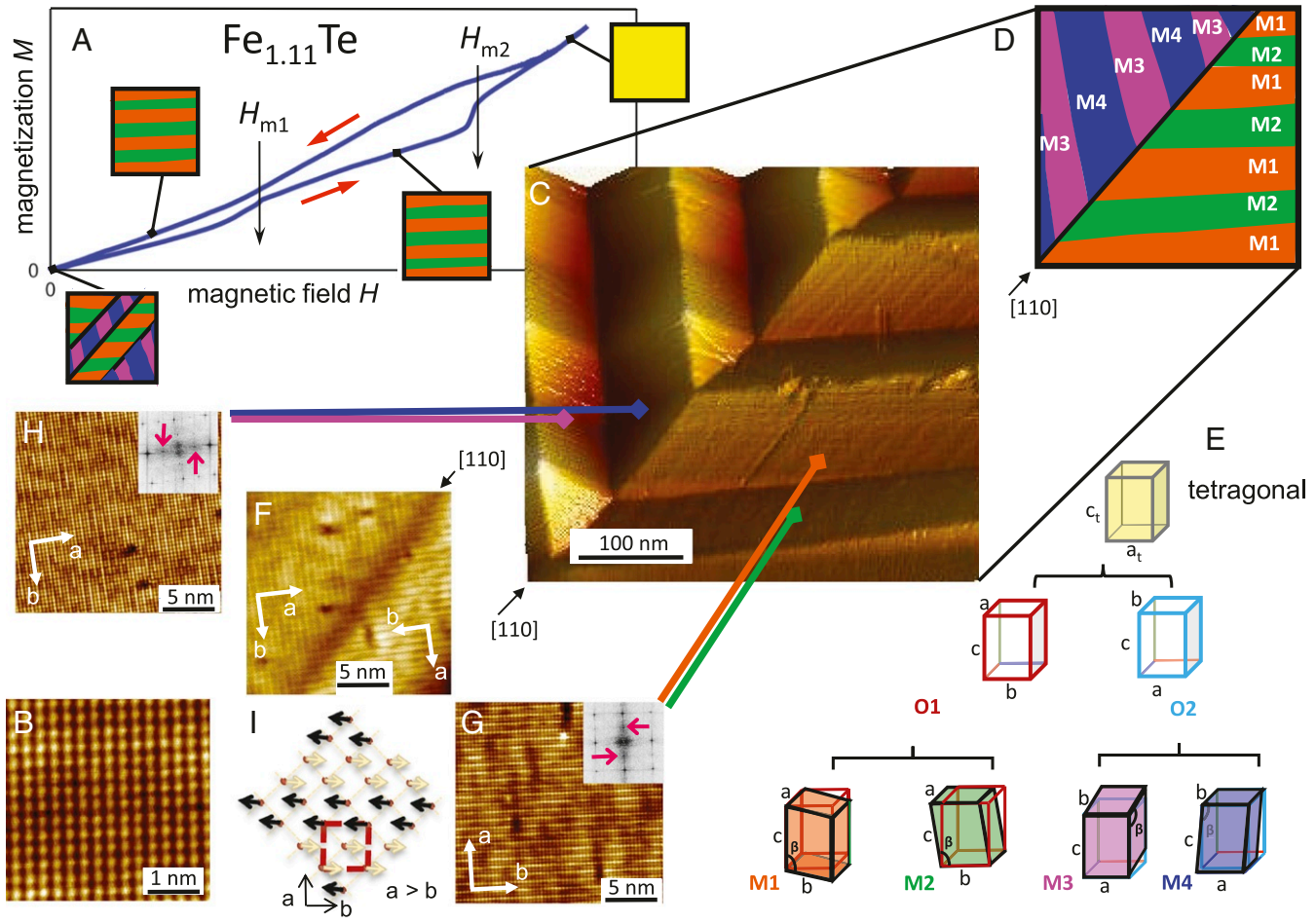

Fig. 1. The field-induced solid–solid transformation processes and underlying microstructure of a $Fe_{1.11}Te$ single crystal. (*A*) Magnetization $M(H)$ obtained at 48 K up to a magnetic field of 58 T (see Fig. 2 for details). *Insets* show schematics of the microstructural change upon applying a magnetic field. (*B*) Topography on an area of 5 × 5 nm^2 measured at 100 K. (*C*) Three-dimensional topography on an area of 400 × 400 nm^2 at 40 K indicating a hierarchical twin microstructure of the monoclinic phase. (*D*) Cartoon of the topography presented in *C*. (*E*) Schematic unit cells of 4 different twin variants M1 to M4 in the monoclinic phase derived from the 2 orthorhombic variants O1 and O2 describing the *ab* and *ba* deformation of the tetragonal parent lattice. (*F*) Topography on an area of 20 × 20 nm^2 depicting a twin-domain wall along the [110] direction across which a periodic modulation of a 1D density wave oriented at an angle of $\approx 90^\circ$ with respect to each other can be seen. (*G* and *H*) STM topography on areas of 20 × 20 nm^2 on either side of a [110] twin-domain wall. *Insets* display corresponding Fourier transformations. The pink arrows highlight additional spots at (0, 0.5) and (0.5, 0), respectively, confirming the 1D stripe structure. The color-coded arrows (blue, pink, orange, and green) point to the corresponding domains in *C* and *D*. (*I*) Schematic in-plane spin structure of $Fe_{1.11}Te$ in the monoclinic phase. The red rectangle represents the *ab* plane of the unit cell; black and yellow arrows indicate the orientation of the spins at the individual Fe sites.

field-polarized, effectively paramagnetic tetragonal phase (Fig. 1*A*, *Right Inset*). A scanning tunneling microscope (STM) was used to determine the twin microstructure, which is shown to fulfill the conditions for self-accommodation of the spontaneous strains at the ferroelastic tetragonal-to-monoclinic transition. The hierarchical arrangement of monoclinic twin domains is identified as a crossing twin pattern described by the continuum theory of martensites (12, 13). Using density functional theory (DFT) calculations, we identified $[10\bar{1}]$ of the monoclinic twin variants as the easy axis, which corresponds to a direction in one of the ac planes of the tetragonal lattice structure. Our experiments provide direct evidence for a giant magnetoelastic coupling in an antiferromagnet, which is closely related to an Fe-based superconductor, namely FeSe.

Results

Scanning Tunneling Microscopy. Since the martensitic microstructure is a salient feature of the materials displaying the MSM effect, we first investigated the microstructure of a $Fe_{1.11}Te$ single crystal using a low-temperature STM. $Fe_{1.11}Te$ exhibits a direct tetragonal-to-monoclinic phase transition (14, 15) (*SI Appendix*, sections 1 and 2) and is, hence, prone to strong MSM effects. Cleaving the $Fe_{1.11}Te$ crystal in situ exposes Te-terminated surfaces which may contain different amounts of excess Fe (*SI Appendix*, section 3). In the following, Te-terminated clean surfaces are presented, since they allow us to examine the microstructure. In Fig. 1*B*, a STM topographic image of $Fe_{1.11}Te$ over an area of 5 × 5 nm^2 taken in the tetragonal phase at 100 K is displayed. The atomically resolved surface with $a_{Te-Te} \approx 3.8$ Å is consistent with the bulk lattice parameter (*SI Appendix*, section 4). In the monoclinic phase, 4 differently oriented twin variants M1 to M4 are expected (16), which can be discerned from Fig. 1 *C* and *D* while Fig. 1*E* depicts how these 4 variants are brought about. The STM topography over a large area of 400 × 400 nm^2 measured at 40 K, a temperature well below the tetragonal-to-monoclinic structural phase transition, reveals all of the 4 twin variants (Fig. 1*C*). The surface morphology indicates a hierarchical twinning (17) resembling a chevron pattern with the domain orientation described in Fig. 1 *D* and *E*. A similar twinning pattern has been recently reported

for $Fe_{1.08}Te$ (18). In Fig. 1*C*, an invariant twin plane (110) running along the [110] direction distinguishes domains in which the crystallographic a and b axes are rotated by ≈90°. A typical distance between 2 [110] twin-domain walls is found to be ≈340 nm (*SI Appendix*, section 3). Across the (110) invariant twin plane, a further microstructural feature has been observed originating from the alternating monoclinic angle β between c and a axes, approximately, at a distance of about 80 nm. This highly regular pattern of crossing twins is the expected self-accommodating martensitic microstructure that combines all 4 monoclinic variants (12, 13); see *SI Appendix*, sections 5 and 6 for details. In Fig. 1*F*, the STM topographic image of 20 × 20 nm^2 with a [110] twin boundary is presented. In addition to atomic modulation, the image displays 1D stripe structures, which are rotated by ≈90° across the [110] twin boundary. In Fig. 1 *G* and *H*, STM topographic images on either side of a [110] twin boundary are presented. *Insets* show corresponding Fourier transformations. Besides the regular Bragg spots, the 1D charge modulation can be seen from satellite spots at $\mathbf{q} = (0, 0.5)$ and $\mathbf{q} = (0.5, 0)$ which correspond to 2 different twin domains. The period of the stripes in real space is found to be $2a_{Te-Te}$. This is identical to the antiferromagnetic wave vector $\mathbf{q}_{AFM}$ = (0.5, 0) (19) defined in reciprocal space. The AFM wave vector in $Fe_{1.11}Te$ propagates along the a axis, i.e., along the (π,0) direction (19, 20) as schematically represented in Fig. 1*I*. Note that the arrows in Fig. 1*I* indicate individual Fe sites whereas in the STM topography we see Te termination. The 1D stripe structure found here is consistent with results from previous STM experiments conducted with both normal (21–24) and spin-polarized tips (25, 26). In contrast to a charge density wave occurring at $2\mathbf{q}_{AFM}$ expected from the magnetostriction, the 1D stripe order found here at the same wave vector as the $\mathbf{q}_{AFM}$ likely stems from the bond order wave induced by the ferro-orbital ordering taking place at the magneto-structural phase transition (24, 27). This scenario evokes an intertwining of spin, charge, lattice, and orbital degrees of freedom. Further, both the SDW and the CDW domains adapt to the underlying martensitic microstructure.

Magnetization and Magnetostriction. The presence of modulated martensitic phases suggests that the twin boundaries may be easily movable by the application of external magnetic fields (17). To establish this, we performed magnetization $M(H)$ and magnetostriction $\Delta l(H)/l$ measurements in pulsed magnetic fields up to 60 T. The $M(H)$ measurements with magnetic fields H applied along different crystallographic directions of $Fe_{1.11}Te$ are presented in Fig. 2 *A* and *B*. The first measurement was conducted at 1.6 K, after cooling the sample from room temperature, annotated as virgin measurement. When the magnetic field was applied along the tetragonal $[100]_T$ direction (Fig. 2*A*), the $M(H)$ displays a jump at $\mu_0 H_{m1} \approx 48$ T upon increasing the magnetic field. This jump is absent in the decreasing part of the field cycle. With a second field pulse, no anomaly, rather a monotonic behavior, was observed during the entire field pulse. The virgin curve could be recovered only after the sample was heated to a temperature above the temperature of the structural transition (57 K) and cooled back again. This behavior indicates that the jump involves an irreversible structural process, related to the monoclinic phase, and is reminiscent of a memory effect: The sample remembers the first pulse, as long as it is kept below the temperature of the structural phase transition. We also measured $M(H)$ with the magnetic field applied along $[110]_T$ and $[001]_T$ directions. As depicted in Fig. 2*B*, no effect is seen in $M(H)$ up to 60 T, indicating that the jump occurs only when the field is parallel to the $[100]_T$ direction. Fig. 2*C* shows $M(H)$ measured with $H \parallel [100]_T$

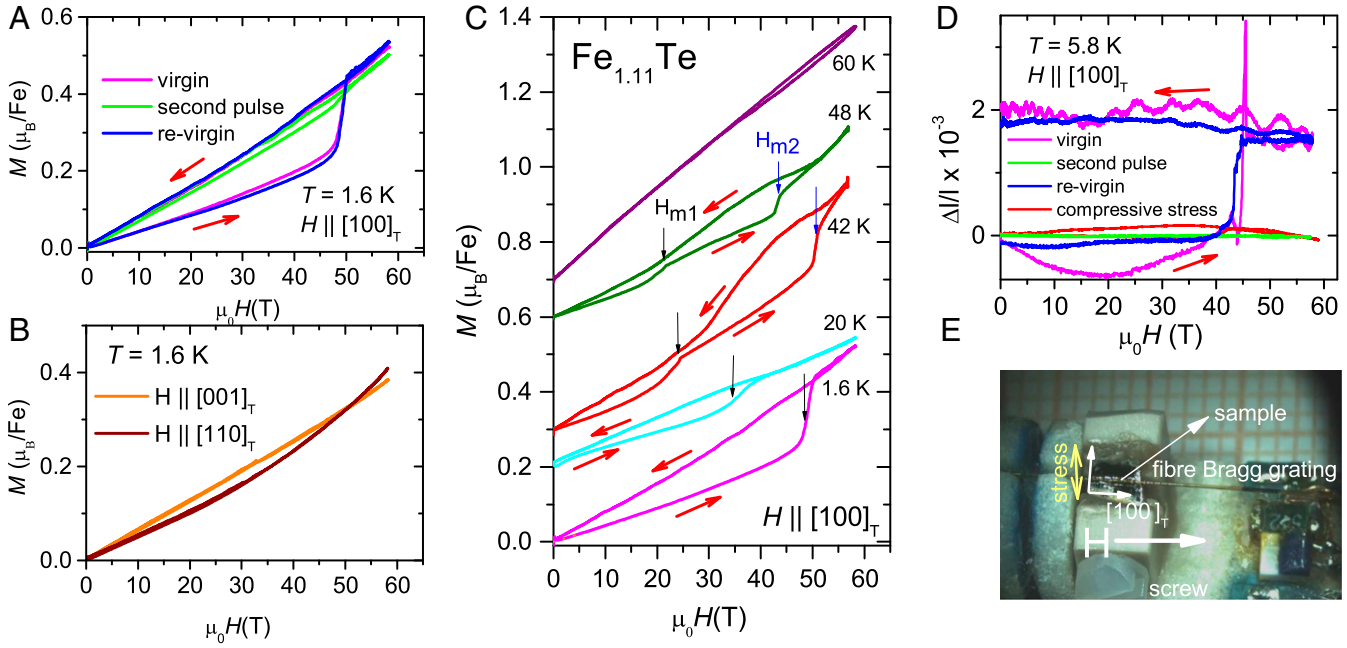

Fig. 2. Magnetization $M(H)$ and magnetostriction $\Delta l(H)/l$ measurements on $Fe_{1.11}Te$. (*A*) $M(H)$ with magnetic field $H \parallel [100]_T$ direction of the tetragonal structure at 1.6 K after cooling the sample from room temperature (virgin) in 0 field, by giving a second field pulse at 1.6 K (second pulse), and after heating the sample to 100 K followed by cooling to 1.6 K (revirgin). (*B*) $M(H)$ curves with $H \parallel [110]_T$ and $H \parallel [001]_T$ directions at 1.6 K. (*C*) $M(H)$ measured at different temperatures. The black arrows indicate the decrease in detwinning field H_{m1} upon increasing temperature. At 42 K, a second jump in $M(H)$ is visible at a field of $\mu_0 H_{m2} \approx$ 50 T, which corresponds to a metamagnetic reverse transformation (main text). The curves measured at 20 K and above are vertically shifted for clarity. (*D*) $\Delta l(H)/l$ measured along the $[100]_T$ direction. The jump is absent in the second measurement, confirming an antiferromagnetic shape-memory effect. In *D*, $\Delta l(H)/l$ of a detwinned (by compressive strain) crystal is presented. For all measurements, the magnetic field was kept parallel to the $[100]_T$ crystallographic direction. (*E*) Setup used for the application of compressive stress along $[010]_T$ to mechanically detwin the crystal.

at different temperatures. With increasing temperature, the field H_{m1} decreases and finally it is not observed at and above 60 K. However, at 42 K, while the field is increasing, a second transition appears in a field of $\mu_0 H_{m2} \approx 50$ T. The field H_{m2} also decreases with increasing temperature and disappears at 60 K. Thus, at temperatures near 42 K, $Fe_{1.11}Te$ undergoes 2 different types of field-induced reorientations. Similar discontinuities have been previously reported in $Fe_{1.1}Te$ by Knafo et al. (10). In the following, we show that H_{m1} and H_{m2} are the critical fields required for detwinning and a reverse phase transformation into a spin–polarized tetragonal phase, respectively.

First we address the process occurring at field H_{m1}. To this end, we performed magnetostriction experiments (28) on both twinned and mechanically detwinned $Fe_{1.11}Te$ single crystals (29–31). The virgin curve measured after cooling the sample from room temperature to 5.8 K displays a jump in $\Delta l(H)/l$ at $\mu_0 H_{m1} \approx 45$ T, as can be seen in Fig. 2*D*. During the second magnetic pulse at 5.8 K, no change in sample length was observed. This result is consistent with the $M(H)$ behavior and confirms the magnetic shape-memory effect; i.e., the change in the shape of the sample induced by the first field pulse is persistent. The virgin behavior could be recovered if the sample is heated above the structural transition temperature (blue curve in Fig. 2*D*). In a subsequent measurement, we mounted the same sample on a simple strain device shown in Fig. 2*E*. This allows for applying a compressive stress along the $[010]_T$ direction, which prevents the twin-domain formation once the sample is cooled below the structural transition. In result, the change in length upon applying a field pulse is significantly suppressed at H_{m1} (red curve in Fig. 2*D*). The $H-T$ diagram of $Fe_{1.11}Te$ is presented in *SI Appendix*, section 7.

Now we focus on the second reorientation transition occurring at field H_{m2}. For this purpose, we use an $Fe_{1.12}Te$ crystal (Fig. 3*A*). At 1.6 K and $H \parallel [100]_T$ in the virgin measurement, 2 distinct transitions are visible at $\mu_0 H_{m1} \approx 42$ T and $\mu_0 H_{m2} \approx 52$ T. In contrast to H_{m1}, however, the jump at H_{m2} is also present when the magnetic field is applied parallel to the $[110]_T$ as well as the $[001]_T$ directions (Fig. 3 *B* and *C*), indicating that the second transition is isotropic and involves a different mechanism. According to the $\Delta l(H)/l$ measurements at H_{m1}, the sample expands along the a axis due to detwinning, but at H_{m2}, the sample shrinks (Fig. 3*D*). Since the lattice parameter a in the tetragonal phase is smaller than that in the monoclinic phase (15), contraction in the sample length at H_{m2} indicates that the material undergoes a transformation toward the tetragonal phase at H_{m2}. This structural transformation has also been observed in $Fe_{1.1}Te$ (11). The irreversible behavior at H_{m2} indicates that the second transition also involves a memory effect. However, the behavior can be recovered during the second pulse; i.e., the sample is not required to be heated above the structural transition temperature. The system returns to the distorted martensitic state within the waiting time (1 h in the case of magnetization and 4 h in the case of magnetostriction measurements) after the magnetic pulse necessary to cool down the pulsed-field magnet. To obtain the temperature dependence of H_{m2}, we performed $\mathrm{d}l(H,T)/l$ also on mechanically detwinned crystals. H_{m2}

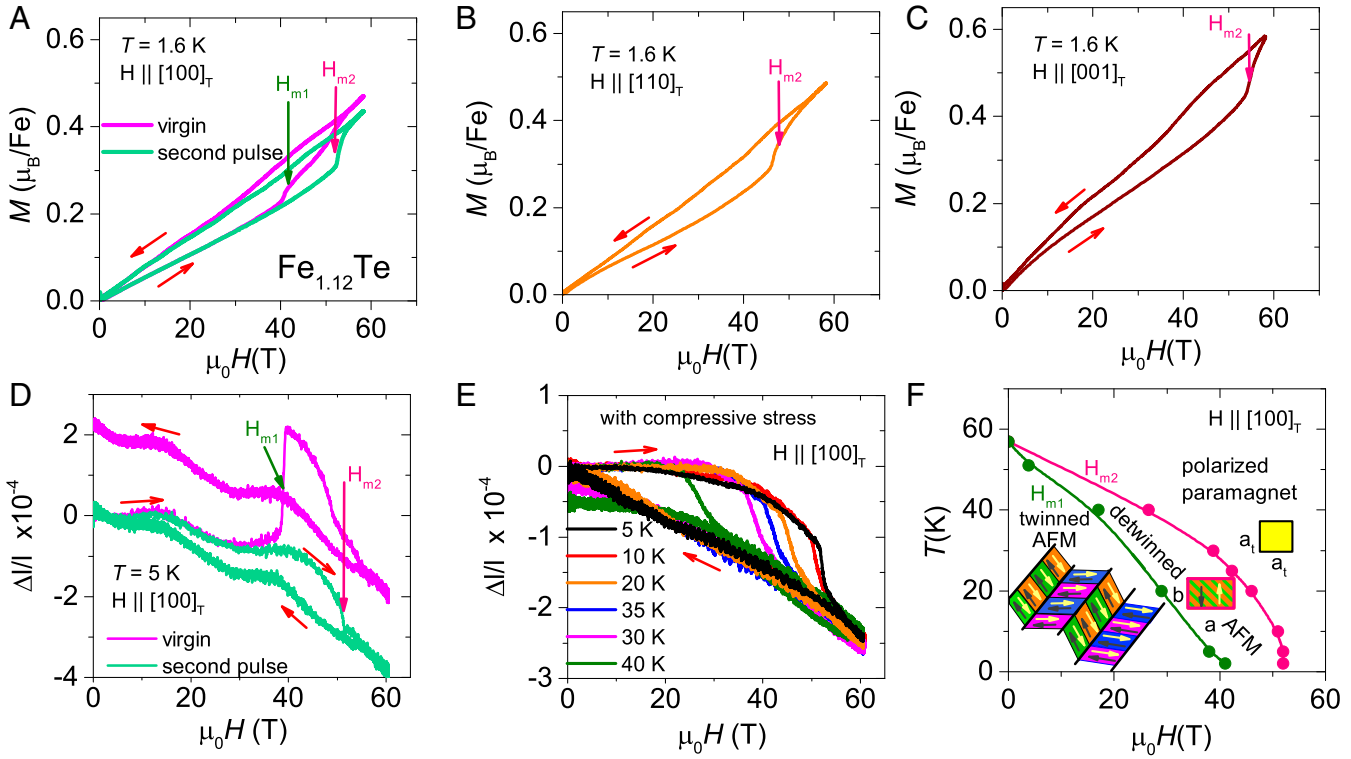

Fig. 3. Magnetization $M(H)$ and magnetostriction $\Delta l(H)/l$ measurements on $Fe_{1.12}Te$. (*A*) $M(H)$ curves measured with applied magnetic field $H \parallel [100]_T$ direction of the tetragonal structure at 1.6 K after cooling the sample from room temperature (virgin) in 0 field and by applying a second field pulse at 1.6 K (second pulse). (*B*) $M(H)$ curve with applied field $H \parallel [110]_T$ at 1.6 K. (*C*) $H \parallel [001]_T$ direction at 1.6 K. (*D*) $\Delta l(H)/l$ measured along the $[100]_T$ direction, both during the first (virgin) pulse and during the second pulse. The magnetic field H was kept parallel to the $[100]_T$ crystallographic direction. (*E*) $\Delta l(H)/l$ measured along $[100]_T$ at different temperatures on mechanically detwinned crystals. (*F*) Magnetic field vs. temperature phase diagram of $Fe_{1.12}Te$ with $H \parallel [100]_T$ displaying a field-induced transformation of a martensite (twinned phase) to austenite via a detwinned martensite phase, i.e., an effectively single-variant orthorhombic state, which however still can be nanotwinned into 2 monoclinic variants (shown in *Inset*).

decreases with increasing temperature as seen in Fig. 3*E*. Fig. 3*F* depicts the field-temperature phase diagram for $Fe_{1.12}Te$ showing a field-dependent transformation from martensite to austenite via a distorted martensitic state upon increasing magnetic field. None of these effects were observed in $Fe_{1.14}Te$ up to 60 T (*SI Appendix*, section 8). This confirms that the MSM effects in $Fe_{1+y}Te$ for $y < 0.14$ rely on the ferroelastic tetragonal-to-monoclinic transformation.

Density Functional Theory. To gain a reasonable estimate of the strength of the magnetocrystalline anisotropy and the direction of the easy axis, we used fully relativistic DFT calculations (32). Since $Fe_{1+y}Te$ is a $3d$-transition metal compound with a relatively stable spin moment on Fe, the magnetocrystalline anisotropy is well described by DFT calculations. The leading contribution to the effective anisotropy in this compound, i.e., squared in Cartesian components of the unit staggered vector $\mathbf{l} = (l_1, l_2, l_3)$, has the form $w_a = K_1(l_1)^2 + K_2(l_2)^2 + K_3(l_3)^2$. This describes a system with 3 different and orthogonal anisotropy axes designating easy, intermediate, and hard directions for the antiferromagnetic double-striped ground state. It is found that this form describes the numerical data from the DFT results fairly well (*SI Appendix*, section 9). The easy axis is in the ac plane, approximately in the monoclinic $[10\bar{1}]_M$ direction and the intermediate axis is along b, while the hard axis again is in the ac plane close to the $[101]_M$ directions. The DFT values for the magnetic anisotropy from the energy difference for the antiferromagnetic ground state with moments pointing in the hard (intermediate) axis direction compared to moments along the easy direction are found to be 1.7 (1.3) meV/Fe atom. This gives then a magnetocrystalline anisotropy of 6.0 (4.6) MJ/m^3 for the energy difference between $\mathbf{l}$ in the easy and the hard (the easy and the intermediate) direction, which determines a spin-flop field. These are large values and the applied fields up to 60 T are not able to reach a spin-flop field (*SI Appendix*, section 10). Therefore, the difference in magnetic free energy in the different variants in an applied field will be essentially dictated by the difference in the Zeeman energy resulting from the net magnetization, which differs in the differently oriented twin variants. At the onset of the MSM $\mu_0 H_{m1} = 48$ T, we can estimate this difference as about 0.2 μ_B/ Fe atom (at the lowest temperature, Fig. 2*A*, assuming that the lower branch of $M(H)$ reflects the magnetization process of a 50:50 mixture of hardly and easily magnetized variants, while the upper branch reflects the magnetization response of the detwinned state). This free energy difference between the variants then gives the critical stress $\sigma_0 \simeq 1.6$ MPa, which is able to overcome the pinning of twin walls and set them into motion. This is a relatively small value of critical stress, comparable to the values of about 2 MPa reported for ferromagnetic Ni_2MnGa MSM materials (33).

Shape-Memory Behavior in Related Compounds. The description of the different magnetic-field–driven lattice transformations highlights the importance of self-accommodation (12, 13) and the cross-twinned microstructure (Fig. 1). Shape-memory effects of the kind reported here require a tetragonal-to-monoclinic or -triclinic transformation and vanishing volume mismatch between the phases. This invites a discussion about the possibilities to observe similar anomalous lattice effects in other materials from the class of high-temperature Fe-based superconductors with structural instability. Some systems like NaFeAs (34, 35) or $BaFe_2As_2$ (29, 36) can be detwinned by applying mechanical stresses. Magnetic-field–driven detwinning has been reported only for a few particular Fe–pnictide systems (6–8). As these materials generically undergo tetragonal-to-orthorhombic phase transitions, only 2-variant twinning occurs and the accommodation of the spontaneous strains is hampered. In these systems, no easy path for solid–solid transformations via multivariant twinning and for variant reorientation under the small pressure from magnetic forces is available. In $Ba(Fe_{1-x}Co_x)_2As_2$, a magnetic-field–driven detwinning has been observed (8). However, this system is not tetragonal, but orthorhombic at room temperature, and the structural phase transition seems to imply a modulation of the lattice (37). Possibly, the observed detwinning relies on a strain-glass–like microstructure due to disorder effects in this alloyed system. The observation of field-driven detwinning in $EuFe_2As_2$ (6, 7) is exceptional. It is based on a particular antiferromagnetic order and an intricate mechanism involving the large magnetic moment of Eu combined with magnetoelastic coupling of the Fe sublattice (38), but the evolution of microstructure during this process is unknown at present. Recently, the possibility of thermal shape-memory effects and anomalously large, "superelastic" strains has been demonstrated for micropillars of $CaFe_2As_2$ (39). The extremely large spontaneous strains of order 10% in $CaFe_2As_2$ stem from an entirely different mechanism, namely, an isostructural tetragonal-to-collapsed tetragonal transition under pressure. A shape-memory behavior then requires one to exploit also the symmetry-breaking martensitic transition at ambient pressure, which however seems to be associated with plastic deformations. Notably, $Fe_{1+y}Te$ displays a similar isostructural, so-called type-0, transition from tetragonal-to-tetragonal phase under pressure. The high-pressure phase, however, is ferrromagnetic (40). Cycling applied pressure, temperature, and an additional magnetic field for the transition from the monoclinic ground state to this tetragonal ferromagnetic phase in $Fe_{1+y}Te$, similar to the cycle proposed in the work by Sypek et al. (39), may offer a way to a magnetic-field control of this type of superelasticity and shape-memory effects.

Conclusions

The field-induced detwinning in $Fe_{1+y}Te$, which is structurally related to the Fe-based superconductors, underlines the relevance of spin–orbit coupling in inducing a giant magnetoelastic coupling. As a corollary of our study an intriguing question arises: Whether the presence of magnetic shape-memory effects in 2 materials which are closely related to high-T_c superconductors, namely, the cuprates and the Fe-based superconductors, is just a coincidence or whether spin–orbit interaction is one of the necessary ingredients for high-T_c superconductivity. This implies the coupling of electrons and phonons via the spin channel, which is considered an important constituent for superconductivity in Fe–pnictide superconductors (41). Such an underlying commonality of shape-memory effects in members of 2 classes of high-T_c materials is expected to trigger future inquiry regarding the role of elastic degrees of freedom and anisotropic spin–lattice couplings for the mechanism of high-T_c superconductivity.

Materials and Methods

Single crystals of $Fe_{1+y}Te$ (y = 0.11, 0.12, and 0.14) were grown using chemical vapor transport (CVT) with iodine as a transport reagent (42, 43) (*SI Appendix*, section 2). For STM, conducted at a base temperature of 4.5 K and in ultrahigh vacuum, single crystals were cleaved in situ at ≈25 K. The $M(H)$ and the $\Delta l(H)/l$ measurements were performed in the pulsed magnetic fields up to 60 T at the high magnetic-field laboratory in Dresden-Rossendorf (HLD-EMFL). The DFT calculations were done using fplo14.00 (32), using the generalized gradient approximation (GGA) in the PBE parameterization as an exchange-correlation functional.

ACKNOWLEDGMENTS. We thank Ulrike Nitzsche for computational assistance, Sebastian Fähler for critical reading of the manuscript, and L. H. Tjeng for fruitful discussions. We acknowledge the support of the Dresden High Magnetic Field Laboratory (HLD-EMFL), Helmholtz-Zentrum Dresden-Rossendorf, a member of the European Magnetic Field Laboratory (EMFL). Financial support from the Deutsche Forschungsgemeinschaft within the Schwerpunktprogramm SPP1458 is gratefully acknowledged.

1. K. Ullakko, J. K. Huang, C. Kantner, R. C. O'Handley, V. V. Kokorin, Large magnetic field-induced strains in Ni_2MnGa single crystals. *Appl. Phys. Lett.* **69**, 1966–1968 (1996).
2. R. C. O'Handley, S. J. Murray, M. Marioni, H. Nembach, S. M. Allen, Phenomenology of giant magnetic-field-induced strain in ferromagnetic shape-memory materials. *J. Appl. Phys.* **87**, 4712–4717 (2000).
3. R. Kainuma *et al.*, Magnetic-field-induced shape recovery by reverse phase transformation. *Nature* **439**, 957–960 (2006).
4. A. N. Lavrov, S. Komiya, Y. Ando, Magnetic shape-memory effect in a crystal. *Nature* **418**, 385–386 (2002).
5. S. Raasch *et al.*, Magnetic shape memory effect in the paramagnetic state in RCu_2 (R=rare earth) antiferromagnets. *Phys. Rev. B* **73**, 064402 (2006).
6. Y. Xiao *et al.*, Field-induced spin reorientation and giant spin-lattice coupling in $EuFe_2As_2$. *Phys. Rev. B* **81**, 220406(R) (2010).
7. S. Zapf *et al.*, Persistent detwinning of iron-pnictide $EuFe_2As_2$ crystals by small external magnetic fields. *Phys. Rev. Lett.* **113**, 227001 (2014).
8. J. P. C. Ruff *et al.*, Susceptibility anisotropy in an iron arsenide superconductor revealed by X-ray diffraction in pulsed magnetic fields. *Phys. Rev. Lett.* **109**, 027004 (2012).
9. M. Tokunaga, T. Kihara, Y. Mizuguchi, Y. Takano, Field-induced magnetostructural transitions in antiferromagnetic $Fe_{1+y}Te_{1-x}S_x$. *J. Phys. Soc. Jpn.* **81**, 063703 (2012).
10. W. Knafo *et al.*, High-field irreversible moment reorientation in the antiferromagnet $Fe_{1.1}Te$. *Phys. Rev. B* **87**, 020404 (2013).
11. X. Fabrèges *et al.*, Field-induced structural transition and irreversible domain detwinning in the antiferromagnet $Fe_{1.1}Te$. *Phys. Rev. B* **95**, 174434 (2017).
12. K. Bhattacharya, Self-accommodation in martensite. *Arch. Ration. Mech. Anal.* **120** 201–244 (1992).
13. K. Bhattacharya, *Microstructure of Martensite: Why It Forms and How It Gives Rise to the Shape-Memory Effect* (Oxford University Press, 2003).
14. S. Rößler *et al.*, First-order structural transition in the magnetically ordered phase of $Fe_{1.13}Te$. *Phys. Rev. B* **84**, 174506 (2011).
15. C. Koz, S. Rößler, A. A. Tsirlin, S. Wirth, U. Schwarz, Low-temperature phase diagram of $Fe_{1+y}Te$ studied using x-ray diffraction. *Phys. Rev. B* **88**, 094509 (2013).
16. M. Mamivand, M. A. Zaeem, E. E. Kadiri, L.-Q. Chen, Phase field modeling of the tetragonal-to-monoclinic phase transformation in zirconia. *Acta Mater.* **61**, 5223–5235 (2013).
17. R. Niemann *et al.*, The role of adaptive martensite in magnetic shape memory alloys. *Add. Eng. Mater.* **14**, 562–581 (2013).
18. J. Warmuth, M. Bremholm, P. Hofmann, J. Wiebe, R. Wiesendanger, Domain imaging across the magneto-structural phase transition in $Fe_{1+y}Te$. *NPJ Quantum Mater.* **3**, 21 (2018).
19. W. Bao *et al.*, Tunable $(\delta\pi, \delta\pi)$-type antiferromagnetic order in α-Fe(Te,Se) superconductors. *Phys. Rev. Lett.* **102**, 247001 (2009).
20. E. E. Rodriguez *et al.*, Magnetic-crystallographic phase diagram of the superconducting parent compound $Fe_{1+x}Te$. *Phys. Rev. B* **84**, 064403 (2011).
21. T. Machida *et al.*, Unidirectional electronic structure in the parent state of iron-chalcogenide superconductor $Fe_{1+\delta}Te$. *J. Phys. Soc. Jpn.* **81**, 074714 (2012).
22. A. Sugimoto, R. Ukita, T. Ekino, Nano-scale stripe structures on FeTe observed by low-temperature STM/STS. *Phys. Procedia* **45**, 85–88 (2013).
23. A. Sugimoto, R. Ukita, A. M. Gabovich, Variable electronic stripe structures of the parent iron-chalcogenide superconductor $Fe_{1+d}Te$ observed by STM-STS. *Phys. Rev. B* **90**, 224503 (2014).
24. W. Li *et al.*, Charge ordering in stoichiometric FeTe: Scanning tunneling microscopy and spectroscopy. *Phys. Rev. B* **93**, 041101(R) (2016).
25. M. Enayat *et al.*, Real-space imaging of the atomic-scale magnetic structure of $Fe_{1+y}Te$. *Science* **345**, 653–656 (2014).
26. T. Hänke *et al.*, Reorientation of the diagonal double-stripe spin structure at $Fe_{1+y}Te$ bulk and thin-film surfaces. *Nat. Commun.* **8**, 13939 (2017).
27. D. Fobes *et al.*, Ferro-orbital ordering transition in iron telluride $Fe_{1+y}Te$. *Phys. Rev. Lett.* **112**, 187202 (2014).
28. R. Daou *et al.*, High resolution magnetostriction measurements in pulsed magnetic fields using fiber Bragg gratings. *Rev. Sci. Instrum.* **81**, 033909 (2010).
29. I. R. Fisher, L. Degiorgi, Z. X. Shen, In-plane electronic anisotropy of underdoped "122" Fe arsenide superconductors revealed by measurements of detwinned single crystals. *Rep. Prog. Phys.* **74**, 124506 (2011).
30. J. Jiang *et al.*, Direct in-plane resistivity anisotropy in a detwinned FeTe single crystal: Evidence for a Hund's metal. *Phys. Rev. B* **88**, 115130 (2013).
31. T. Nakajima *et al.*, Two kinds of in-plane resistivity anisotropy in $Fe_{1+\delta}Te$ ($\delta = 0.09$) as seen via synchrotron radiation x-ray diffraction and *in situ* resistivity measurements. *Phys. Rev. B* **91**, 205125 (2015).
32. K. Koepernik, H. Eschrig, Full-potential nonorthogonal local-orbital minimum-basis band-structure scheme. *Phys. Rev. B* **59**, 1743–1757 (1999).
33. R. C. O'Handley, Model for strain and magnetization in magnetic shape-memory alloys. *J. Appl. Phys.* **83**, 3263–3270 (1998).
34. Y. Zhang *et al.*, Symmetry breaking via orbital-dependent reconstruction of electronic structure in detwinned NaFeAs. *Phys. Rev. B* **85**, 085121 (2012).
35. Y. Li *et al.*, Coupling and nematic fluctuations in NaFeAs. *Phys. Rev. X* **8**, 021056 (2018).
36. J. H. Chu *et al.*, In-plane resistivity anisotropy in an underdoped iron arsenide superconductor. *Science* **329**, 824–826 (2010).
37. C. Cantoni *et al.*, Room-temperature $Ba(Fe_{1-x}Co_x)_2As$ is not tetragonal: Direct observation of magnetoelastic interactions in pnictide superconductors. *Adv. Mater.* **27**, 2715–2721 (2015).
38. J. Maiwald, I. I. Mazin, P. Gegenwart, Microscopic theory of magnetic detwinning in iron-based superconductors with large-spin rare earths. *Phys. Rev. X* **8**, 011011 (2018).
39. J. T. Sypek *et al.*, Superelasticity and cryogenic linear shape memory effects of $CaFe_2As_2$. *Nat. Commun.* **8**, 1083 (2017).
40. K. Mydeen *et al.*, Pressure-induced ferromagnetism due to an anisotropic electronic topological transition in $Fe_{1.08}Te$. *Phys. Rev. Lett.* **119**, 227003 (2017).
41. T. Egami, B. V. Fine, D. Parshall, A. Subedi, D. J. Singh, Spin-lattice coupling and superconductivity in Fe pnictides. *Adv. Condens. Matter Phys.* **2010**, 164916 (2010).
42. C. Koz, "Investigations on the parent compounds of Fe-chalcogenide superconductors," PhD thesis, Technische Universität Dresden, Germany (2016).
43. S. Rößler, C. Koz, S. Wirth, U. Schwarz, Synthesis, phase stability, structural, and physical properties of 11-type iron chalcogenides. *Phys. Status Solidi B* **254**, 1600149 (2017).